LiQSS: Post-Transformer Linear Quantum-Inspired State-Space Tensor Networks for Real-Time 6G

Farhad Rezazadeh, *Member, IEEE*, Hatim Chergui, *Senior Member, IEEE*, Amir Ashtari Gargari, *Member, IEEE*, Mehdi Bennis, Houbing Song, Lingjia Liu, and Merouane Debbah, *Fellow, IEEE*

arXiv:2601.12375v3 [cs.NI] 5 Jun 2026

***Abstract*—Proactive and agentic control in Sixth-Generation (6G) Open Radio Access Networks (O-RAN) requires control-grade prediction under stringent Near-Real-Time (Near-RT) latency and computational constraints. While Transformer-based models are effective for sequence modeling, their quadratic complexity limits scalability in Near-RT RAN Intelligent Controller (RIC) analytics. This paper investigates a post-Transformer design paradigm for efficient radio telemetry forecasting. We propose a quantum-inspired many-body state-space tensor network that replaces self-attention with stable structured state-space dynamics kernels, enabling linear-time sequence modeling. Tensor-network factorizations in the form of Tensor Train (TT) / Matrix Product State (MPS) representations are employed to reduce parameterization and data movement in both input projections and prediction heads, while lightweight channel gating and mixing layers capture non-stationary cross-Key Performance Indicator (KPI) dependencies. The proposed model is instantiated as an agentic perceive–predict xApp and evaluated on a bespoke O-RAN KPI time-series dataset comprising 59,441 sliding windows across 13 KPIs, using Reference Signal Received Power (RSRP) forecasting as a representative use case. Our proposed Linear Quantum-Inspired State-Space (LiQSS)[1] model is $10.8\times$–$15.8\times$ smaller and approximately $1.4\times$ faster than prior structured state-space baselines. Relative to Transformer-based models, LiQSS achieves up to a $155\times$ reduction in parameter count and up to $2.74\times$ faster inference, without sacrificing forecasting accuracy.**

***Index Terms*—6G, O-RAN, post-Transformer, state-space models, tensor networks**

I. Introduction

6G mobile networks are expected to natively support intelligent, adaptive, and autonomous control across heterogeneous radio access technologies, extreme densification, and ultra-low latency services [1]. To this end, the O-RAN architecture introduces openness, disaggregation, and programmability as first-class design principles [2], enabling Artificial Intelligence (AI) and Machine Learning (ML) to be deployed as control and optimization functions in the form of xApps and rApps. In particular, the Near-RT RIC, operating at time scales from tens of milliseconds to seconds, is envisioned as a key enabler of proactive and agentic radio resource management in 6G networks.

A fundamental requirement for agentic control in the Near-RT RIC is *control-grade prediction*; the ability to forecast radio telemetry and KPIs accurately and with bounded latency under tight computational and memory constraints. Accurate short-horizon forecasting of KPIs such as RSRP, Signal-to-Interference-plus-Noise Ratio (SINR), and traffic load enables proactive scheduling, mobility management, interference mitigation, and energy optimization. However, Near-RT deployment imposes strict limits on inference latency, model footprint, and data movement, particularly when xApps are co-located with virtualized RAN components and must operate at scale across large numbers of cells and users.

Transformer-based architectures have recently emerged as a dominant paradigm for sequence modeling and time-series forecasting [3]–[10] due to their expressive self-attention mechanism and strong empirical performance across natural language processing, vision, and time-series analysis. Consequently, Transformers and their variants have been explored for radio analytics and network forecasting tasks. Nevertheless, the quadratic time and memory complexity of self-attention with respect to sequence length poses a significant barrier to their adoption in Near-RT RIC environments. This limitation is further exacerbated by the high dimensionality, multivariate nature, and non-stationarity of radio telemetry streams, making naive scaling of Transformer models impractical for real-time 6G control loops.

Motivated by these challenges, our recent research [11], [12] has explored *post-Transformer* sequence modeling paradigms that replace explicit attention mechanisms with structured state-space dynamics. Linear State-Space Models (SSMs) [13], particularly those derived from continuous-time systems and orthogonal polynomial projections, have demonstrated the ability to model long-range temporal dependencies with linear computational complexity. Among these, architectures based on High-order Polynomial Projection Operators (HiPPO) and their Legendre variants [14] enable stable and expressive representations of continuous-time signals while admitting efficient implementations via causal convolutions.

In parallel, tensor network methods [15] originating from quantum many-body physics [16], [17] have gained attention as a principled approach to representing high-dimensional functions with reduced parameterization and controlled expressivity. The TT and MPS decompositions [15], [18], in particular, provide low-rank factorizations that significantly

F. Rezazadeh is with the BrainOmega and the Technical University of Catalonia (UPC), 08028 Barcelona, Spain (e-mail: farhad.rezazadeh@upc.edu).

H. Chergui is with i2CAT Foundation, 08034 Barcelona, Spain (e-mail: hatim.chergui@i2cat.net).

A. shtari Gargari is with the Centre Tecnologic de Telecomunicacions de Catalunya (CTTC/CERCA), 08860 Castelldefels, Spain (e-mail: aashtari@cttc.es).

M. Bennis is with the University of Oulu, 90570 Oulu, Finland (e-mail: mehdi.bennis@oulu.fi).

H. Song is with the University of Maryland, Baltimore County (UMBC), 21250 Baltimore, USA (e-mail: h.song@ieee.org).

L. Liu is with the Virginia Tech, 24061 Blacksburg, USA (e-mail: ljliu@vt.edu).

M. Debbah is with the Khalifa University of Science and Technology, 127788 Abu Dhabi, UAE (e-mail: merouane.debbah@ku.ac.ae).

[1]To support reproducibility, the source code is publicly available for non-commercial use at https://github.com/frezazadeh/quantum-state-space.

TABLE I: Overview of Representative Transformer- and SSM-Based Models for Time-Series.

Model	Architecture	Key Techniques	Target Problems	Limitations / Technical Gaps
Informer [3]	Transformer (efficient attention; encoder–decoder)	ProbSparse self-attention; attention distilling; generative-style decoder	Long sequence time-series forecasting (LSTF)	Still attention-based; long-context compute/memory remains nontrivial
FEDformer [4]	Transformer with decomposition + frequency-domain modeling	Seasonal-trend decomposition; Fourier / wavelet-enhanced blocks	Long-term series forecasting (seasonality/trend + long horizons)	Relies on decomposition and frequency priors; sensitive to mismatch with data characteristics
ETSformer [5]	Transformer-style forecasting model with smoothing components	Exponential Smoothing Attention (ESA) and Frequency Attention (FA)	Time-series forecasting with interpretability	Smoothing-structured bias may limit flexibility for non-ETS dynamics; still Transformer-family complexity
PatchTST [6]	Transformer (patch-based; channel-independent design)	Temporal patching; channel independence (weight sharing across channels)	Long-term multivariate forecasting; representation learning / pretraining	Patch hyperparameter sensitivity; channel-independence can miss cross-variable coupling
Crossformer [7]	Transformer (cross-time + cross-dimension attention; hierarchical encoder–decoder)	Dimension-Segment-Wise (DSW) embedding; Two-Stage Attention	Multivariate forecasting with cross-variable dependencies	Attention-centric and architecture-heavy; compute scales with cross-time/cross-dimension modeling
RWKV [8]	Transformer–RNN hybrid / linear-attention recurrence	Time-mixing + channel-mixing blocks; linear-attention formulation	General sequence modeling (incl. time series)	General-purpose sequence model; limited time-series-specific forecasting validation in the reference
RetNet [9]	Retention network (sequence model with retention mechanism)	Retention with parallel/recurrent/chunkwise computation	General sequence modeling (LLM-focused)	LLM/sequence-model focus; limited time-series forecasting-specific validation and inductive bias discussion
Chronos [10]	Pretrained probabilistic time-series model via LM adaptation	Scaling+quantization tokenization; pretrained Transformer LMs (multiple sizes)	General time-series forecasting (zero-shot / pretrained)	Model size and tokenization/decoding overhead can be costly; larger variants constrain deployment
MS^3M [11]	Structured SSM forecaster (strictly causal)	Multi-scale HiPPO–LegS kernels; Tustin discretization; SE gating; compact GLU mixing	KPI forecasting (one-step; RSRP highlighted)	Scope emphasizes strict causality and next-step prediction; longer-horizon/transfer needs separate study
WM–MS^3M [12]	Agentic world model built on structured SSM mixtures	Action-conditioned generative state-space; dual decoders; MPC/CEM planning	What-if forecasting + short-horizon decision making	World-model + planning stack adds complexity; performance depends on learned dynamics and action constraints

reduce memory footprint and data movement, while preserving the ability to model complex correlations. Despite their theoretical appeal, the integration of tensor networks with state-space sequence models for real-time network intelligence remains largely unexplored.

In this paper, we propose a *quantum-inspired linear state-space tensor network* architecture for efficient radio telemetry forecasting in 6G O-RAN systems. The proposed model replaces self-attention with structured, stable state-space dynamics based on stable HiPPO-LegS kernels, enabling linear-time sequence modeling. We employ tensor network factorizations in both input embeddings and prediction heads to reduce model size and improve computational efficiency. We introduce lightweight channel gating and mixing layers to capture non-stationary cross-KPI interactions without incurring the overhead of full attention mechanisms. Experimental results demonstrate that the proposed approach achieves accuracy competitive with Transformer-based baselines, while significantly reducing inference latency and model footprint. These findings support the viability of post-Transformer, state-space, and tensor-network-based models as enabling technologies for resource-efficient real-time intelligence in future 6G O-RAN deployments.

A. Related Work

1) Transformer-Based Time-Series Models: Transformers have been widely adopted for time-series forecasting due to their ability to model long-range dependencies via self-attention. Early adaptations such as Informer [3] introduced sparse attention mechanisms to mitigate the quadratic complexity of vanilla Transformers. Subsequent studies explored frequency-domain decomposition and inductive biases, including FEDformer [4] and ETSformer [5], which explicitly model trend and seasonal components. More recent architectures have focused on structural modifications of the attention mechanism. PatchTST [6] segments time-series into patches to reduce effective sequence length, while Crossformer [7] captures cross-dimensional dependencies by alternating temporal and feature-wise attention. iTransformer [19] inverts the role of temporal and feature dimensions, enabling efficient modeling of multivariate dependencies. Beyond classical Transformers, alternative attention approximations and recurrent-attention hybrids have been proposed. Performers [20] replaces softmax attention with kernelized random feature maps, RWKV [8] blends recurrent computation with attention-style parameterization, and RetNet [9] introduces exponential decay-based retention to reduce memory overhead. More recently, foundation-style models such as Chronos [10] adapt large pretrained language models (T5/GPT) to time-series forecasting. Despite their strong empirical performance, Transformer-based models suffer from several limitations in Near-RT O-RAN settings: (i) quadratic or near-quadratic scaling with sequence length, (ii) large parameter footprints and memory traffic, and (iii) weak alignment with the physical and dynamical structure of radio telemetry. These limitations significantly hinder deployment within Near-RT RICs, where inference latency and resource efficiency are first-class constraints.

2) Structured State-Space Models for Sequence Modeling: Structured SSMs have recently emerged as a compelling post-Transformer alternative. These models replace attention with linear dynamical systems that admit efficient convolutional or recurrent implementations. A key development in this direction is the use of HiPPO-based [21] operators, which provide stable and expressive representations of continuous-time signals via orthogonal polynomial projections. Building on this foundation, several SSM architectures have demonstrated strong performance on long-sequence tasks with linear complexity. In the context of radio intelligence and agentic control, our previous studies, MS^{3}M [11] introduced multi-scale structured state-space mixtures for Near-RT O-RAN analytics, while WM–MS^{3}M [12] extended this framework toward agentic world modeling and near-real-time reasoning. These studies demonstrated that SSM-based predictors can outperform attention-based models under strict causality and deployment-faithful evaluation pipelines. However, existing SSM approaches still rely on dense linear projections at the input and output layers, which dominate parameter count and memory traffic. Moreover, cross-KPI interactions are typically handled either implicitly or via lightweight heuristics, leaving a gap between expressive multivariate modeling and strict Near-RT efficiency. Table I summarizes representative Transformer- and SSM-based models.

TABLE II: Major Notations and Parameters.

Symbol	Description	Size/Type
Sets, operators, and basic math		
$\mathbb{R},\ \mathbb{C}$	Real and complex numbers	sets
$\mathbb{E}[\cdot],\ \mathrm{Var}[\cdot],\ \mathrm{Cov}[\cdot]$	Expectation, variance, covariance	scalar/matrix
$\mathrm{Tr}(\cdot)$	Trace	scalar
$\mathrm{diag}(\cdot)$	Diagonal matrix from a vector	matrix
$\lVert\cdot\rVert,\ \lvert\cdot\rvert,\ \langle\cdot,\cdot\rangle$	Norm, absolute value, inner product	—
$\odot$	Hadamard (elementwise) product	—
$\mathcal{O}(\cdot)$	Big-O complexity notation	—
$\mathbb{P},\ \mathcal{F}$	Probability measure; σ-algebra	—
Time, indices, and dimensions		
t	Discrete time index	integer
Δt	E2SM-KPM reporting interval / sampling period	scalar
K	Number of monitored KPIs (features)	$\mathbb{Z}_+$
L	Lookback window length	$\mathbb{Z}_+$
H	Forecast horizon (in this paper $H{=}1$)	$\mathbb{Z}_+$
D	Latent width / number of channels	$\mathbb{Z}_+$
B_ℓ	Number of stacked structured SSM blocks	$\mathbb{Z}_+$
N_s	Per-channel SSM state dimension	$\mathbb{Z}_+$
C_m	Number of HiPPO–LegS mixture components per block	$\mathbb{Z}_+$
D_m	ChannelMix hidden width (often $D_m = \alpha D$)	$\mathbb{Z}_+$
α	ChannelMix expansion factor ($D_m = \alpha D$)	scalar
N	Number of windows (samples)	$\mathbb{Z}_+$
B	Batch size	$\mathbb{Z}_+$
$i,\ \ell,\ \tau$	Feature index; time-in-window; lag index	integers
$t^\star$	Target KPI index (e.g., RSRP)	index
Telemetry, windows, and normalization		
$\mathbf{x}_t$	KPI vector at time t	$\mathbb{R}^K$
$\mathbf{X}_t$	Sliding input window ending at t	$\mathbb{R}^{L\times K}$
$\mathbf{u}_\ell$	ℓ-th row of $\mathbf{X}_t$ (one time step)	$\mathbb{R}^K$
y_t	Target KPI scalar at time t (selected KPI)	$\mathbb{R}$
$\hat{y}_{t+1}$	Predicted next-step target	$\mathbb{R}$
$\{(\mathbf{X}_n, \mathbf{y}_n)\}_{n=1}^N$	Windowed dataset	$\mathbf{X}_n \in \mathbb{R}^{L\times K}$
$\rho_{\mathrm{tr}}, \rho_{\mathrm{va}}$	Chronological split ratios (train/val)	scalars
$\mathcal{I}_{\mathrm{tr}}, \mathcal{I}_{\mathrm{va}}, \mathcal{I}_{\mathrm{te}}$	Train/val/test index sets	subsets of $\{1{:}N\}$
$\boldsymbol{\mu}_x, \boldsymbol{\sigma}_x$	Train-only per-feature input mean/std	$\mathbb{R}^K$
μ_y, σ_y	Train-only target mean/std	scalars
$\tilde{\mathbf{X}}, \tilde{y}$	Standardized inputs/target	as $\mathbf{X}, y$
ϵ	Small constant for std clamping	scalar
Latent sequence, blocks, gating, and mixing		
$\mathbf{e}_\ell$	Latent embedding at step ℓ	$\mathbb{R}^D$
$\mathbf{E}$	Latent sequence tensor (batch, time, channel)	$\mathbb{R}^{\lvert\mathcal{B}\rvert\times L\times D}$
$\mathbf{Y}, \mathbf{Z}$	Intermediate block outputs (after conv/gate; after mix)	$\mathbb{R}^{\lvert\mathcal{B}\rvert\times L\times D}$
$\mathbf{h}$	Causal summary (last-step latent)	$\mathbb{R}^{\lvert\mathcal{B}\rvert\times D}$
$\mathrm{LN}(\cdot)$	Layer normalization	map $\mathbb{R}^D \to \mathbb{R}^D$
$\mathrm{Drop}(\cdot)$	Dropout operator	map
p_{do}	Dropout probability	scalar
$\sigma(\cdot)$	Sigmoid nonlinearity (gating)	scalar-wise map
$\mathrm{GELU}(\cdot)$	GELU nonlinearity (ChannelMix)	scalar-wise map
$\mathbf{g}$	Squeeze-and-Excitation (SE) gate (channel gains)	$\mathbb{R}^D$
$\mathbf{q}_\ell$	ChannelMix gate at time step ℓ	$\mathbb{R}^{D_m}$
$W_\uparrow, W_\downarrow$	ChannelMix up/down projections	$\mathbb{R}^{D\times 2D_m},\ \mathbb{R}^{D_m\times D}$
TT/MPS (Tensor Train) linear operators		
TTIn	TT-parameterized input projection $\mathbb{R}^K \to \mathbb{R}^D$	TTLinear
TTHead	TT-parameterized head $\mathbb{R}^D \to \mathbb{R}$	TTLinear
$\mathbf{n}^{\mathrm{in}}, \mathbf{m}^{\mathrm{in}}$	TT input in/out mode factorization	integer vectors
r_{in}	TT rank for input projection	$\mathbb{Z}_+$
$\mathbf{n}^{\mathrm{hd}}, \mathbf{m}^{\mathrm{hd}}$	TT head in/out mode factorization	integer vectors
r_{hd}	TT rank for prediction head	$\mathbb{Z}_+$
HiPPO–LegS state-space kernels (per block/component)		
A_{ct}	Continuous-time HiPPO–LegS generator	$\mathbb{R}^{N_s\times N_s}$
B_{ref}	Reference input vector for HiPPO construction	$\mathbb{R}^{N_s}$
Δt_0	Base initialization for time-step	scalar
γ	Geometric growth factor across mixture components	scalar
$\Delta t^{(b,m)}$	Learned positive step (block b, component m)	$\mathbb{R}_{>0}$
$\bar{A}$	Discretized transition (Tustin)	$\mathbb{R}^{N_s\times N_s}$
$\bar{B}$	Discretized input map (Tustin)	$\mathbb{R}^{D\times N_s}$
$B^{(b,m)}, C^{(b,m)}$	Learned per-channel SSM parameters	$\mathbb{R}^{D\times N_s}$
$D^{(b,m)}$	Learned skip/diagonal term	$\mathbb{R}^D$
$K^{(b,m)}$	Component kernel taps (depthwise conv filter)	$\mathbb{R}^{D\times 1\times L}$
$K^{(b)}$	Mixture-summed kernel $K^{(b)} = \sum_m K^{(b,m)}$	$\mathbb{R}^{D\times 1\times L}$
$k[\tau]$	Kernel tap at lag τ (per channel)	$\mathbb{R}^D$
$\mathrm{conv1d}(\cdot)$	Depthwise causal 1D convolution (groups=D)	operator
Optimization, training loop, and inference metrics		
θ	Model parameters	collection
$\theta^\star$	Best checkpoint parameters	collection
$E_{\max}$	Maximum epochs	$\mathbb{Z}_+$
p	Early-stopping patience	$\mathbb{Z}_+$
η	Learning rate (AdamW)	scalar
λ	Weight decay (AdamW)	scalar
$c_{\max}$	Gradient clipping threshold	scalar
$\mathcal{L}_{\mathrm{tr}}, \mathcal{L}_{\mathrm{va}}$	Train/val loss (MSE in standardized space)	scalars
$\mathcal{L}_{\mathrm{va}}^\star$	Best validation loss	scalar
Complexity-relevant quantities		
H_a	# attention heads (Transformer baseline)	$\mathbb{Z}_+$
d_h	Per-head dimension ($D = H_a d_h$)	$\mathbb{Z}_+$

B. Contributions

Our contributions address the following technical gaps:

- **Gap: quadratic (or near-quadratic) sequence cost in attention-based forecasting.** Transformer forecasters (e.g., Informer/FEDformer/ETSformer/PatchTST/Crossformer and recent variants) rely on attention or attention-like mechanisms, which introduce $\mathcal{O}(L^2)$ memory/compute terms or heavy parameterization that becomes costly as the lookback window L grows and when deployed at scale in Near-RT xApps (Table I). **Solution:** We propose LiQSS, a post-Transformer design that removes self-attention entirely and instead uses structured state-space dynamics with linear-time and linear-memory dependence on L (Section IV-K).
- **Gap: weak dynamical inductive bias for radio telemetry under strict causality.** Many time-series Transformers treat telemetry as generic sequences and learn temporal structure primarily through attention, which is not explicitly aligned with stable continuous-time dynamics and can be insufficiently robust under distribution shifts and non-stationarity typical of radio KPIs (Section I-A). **Solution:** We instantiate stable HiPPO–LegS state-space dynamics as causal depthwise convolutions, and enhance expressivity via a mixture of C_m time scales per block (Algorithms 1–2, Section IV-F and IV-G).
- **Gap: dense input/output projections dominate parameters and memory traffic in efficient sequence models.** Even when temporal backbones are linear-time (structured SSMs), global dense projections at the embedding and head often remain the main source of parameters and data movement, which is undesirable in Near-RT deployments (see SSM baselines in Table I). **Solution:** We compress the largest global operators by replacing dense embedding and readout maps with TT/MPS (Matrix Product Operator (MPO) [22], [23]) factorizations (TTIn/TTHead), yielding rank-controlled global coupling with substantially fewer

parameters (Section IV-D).

- **Gap: modeling cross-KPI interactions typically relies on expensive global attention.** Multivariate forecasting methods often use feature/temporal attention to capture cross-dimension dependence (e.g., Crossformer-style mechanisms), which increases runtime and footprint, and can be misaligned with tight latency budgets (Table I). **Solution:** We introduce lightweight interaction operators—squeeze–excitation gating (window-level reweighting) and token-wise gated ChannelMix (per-time-step coupling)—to capture non-stationary cross-KPI effects without temporal attention (Section IV-H).

The remainder of this paper is organized as follows. Section II introduces the quantum many-body perspective that motivates the proposed approach. Section III describes the O-RAN system model, telemetry acquisition pipeline, and Near-RT prediction task. Section IV presents the proposed LiQSS architecture, including its theoretical foundations, algorithmic formulation, and computational complexity. Section V details the experimental setup, datasets, baselines, and evaluation protocol. Section VI reports and analyzes numerical results, accuracy–efficiency trade-offs, and qualitative prediction behavior. Finally, Section VII concludes the paper. The major notations used throughout the paper are summarized in Table II.

II. Quantum Many-Body Primer

A. From a Single Quantum System to Many-body Structure

A quantum state of a single finite-dimensional system (a site) is a unit vector $|\psi\rangle \in \mathbb{C}^d$. For a collection of L sites, the joint (pure) state lives in the tensor-product Hilbert space [24], [25]

$$\mathcal{H} = \bigotimes_{\ell=1}^{L} \mathbb{C}^{d_\ell},\ |\psi\rangle = \sum_{i_1=1}^{d_1} \cdots \sum_{i_L=1}^{d_L} \psi_{i_1,\ldots,i_L}\ |i_1\rangle \otimes \cdots \otimes |i_L\rangle\,, \tag{1}$$

where the coefficient tensor $\Psi = [\psi_{i_1,\ldots,i_L}]$ has $\prod_{\ell=1}^{L} d_\ell$ complex entries. The exponential growth of degrees of freedom with L is the central computational challenge of *quantum many-body* systems [16], [17].

B. Low-rank Structure via Entanglement

Correlations in quantum mechanics are quantified by *entanglement* [26]. Given a bipartition of sites into $A = \{1,\ldots,k\}$ and $B = \{k+1,\ldots,L\}$, reshape Ψ into a matrix $\Psi_{(i_A),(i_B)} \in \mathbb{C}^{(\prod_{\ell\in A} d_\ell)\times(\prod_{\ell\in B} d_\ell)}$ and apply a Singular Value Decomposition (SVD) [27]

$$\Psi_{(i_A),(i_B)} = \sum_{r=1}^{\chi_k} \sigma_r^{(k)}\, u_r^{(k)}(i_A)\, v_r^{(k)}(i_B)^*, \tag{2}$$

which is the *Schmidt decomposition* [28]. The Schmidt rank $\chi_k = \mathrm{rank}(\Psi_{(i_A),(i_B)})$ and singular values $\{\sigma_r^{(k)}\}$ determine the bipartite entanglement entropy [29]

$$S_k = -\sum_{r=1}^{\chi_k} p_r^{(k)} \log p_r^{(k)}, \qquad p_r^{(k)} = \left(\sigma_r^{(k)}\right)^2 \Big/ \sum_{j=1}^{\chi_k} \left(\sigma_j^{(k)}\right)^2. \tag{3}$$

Many physically relevant states exhibit *limited* entanglement (e.g., area-law behavior [30]), implying that χ_k remains moderate for all cuts. This motivates representing Ψ using factorizations whose intermediate ranks correspond to χ_k.

C. Matrix Product States and Bond Dimension

A canonical low-entanglement representation is the MPS [18], also known (in real-valued ML settings [15]) as the TT decomposition [31]:

$$\psi_{i_1,\ldots,i_L} = \sum_{\alpha_1,\ldots,\alpha_{L-1}} G^{(1)}_{i_1,\alpha_1} G^{(2)}_{\alpha_1,i_2,\alpha_2} \cdots G^{(L)}_{\alpha_{L-1},i_L}, \tag{4}$$

where $\alpha_\ell \in \{1,\ldots,r_\ell\}$ are *bond* indices and $\{r_\ell\}$ are *bond dimensions* (TT ranks). The bond dimensions upper-bound the Schmidt ranks across all bipartitions, $\chi_k \le r_k$, and hence they control correlation capacity; larger ranks admit richer long-range dependencies, while smaller ranks enforce a structured low-correlation prior.

1) From States to Operators—MPO and TT-linear Maps: Forecasting models use linear maps (embeddings and readout) rather than quantum states. The operator analogue of MPS is the MPO [22], [23], identical to a TT-parameterized matrix. Given $W \in \mathbb{R}^{M\times N}$, reshape it into $\mathcal{W} \in \mathbb{R}^{m_1\times\cdots\times m_d\times n_1\times\cdots\times n_d}$ with $M = \prod_{q=1}^{d} m_q$, $N = \prod_{q=1}^{d} n_q$, and write

$$\mathcal{W}(\mathbf{i},\mathbf{j}) = \sum_{r_1,\ldots,r_{d-1}} \prod_{q=1}^{d} \mathcal{G}^{(q)}(r_{q-1}, i_q, j_q, r_q),\ r_0 = r_d = 1, \tag{5}$$

which matches the TT/MPS form used by `TTLinear` in our implementation. The TT rank thus plays the same role as bond dimension in MPO-based quantum simulation; it limits the operator's ability to couple distant factor modes, while drastically reducing parameters from $\mathcal{O}(MN)$ to $\mathcal{O}\Big(\sum_q r_{q-1} m_q n_q r_q\Big)$ [32].

D. Where the "Many-body" Inspiration Enters our Algorithm

Our model is *quantum-inspired* in the following precise sense:

1) **Degrees of freedom (sites).** The latent representation at each time step, $\mathbf{e}_\ell \in \mathbb{R}^D$, is interpreted as D interacting degrees of freedom (analogous to sites in a 1D many-body chain). Temporal evolution is applied per degree of freedom via channel-wise state-space dynamics, yielding a separable *local* evolution component.
2) **Controlled interaction capacity.** Cross-channel interactions are introduced by lightweight coupling operators (gating and gated mixing). These are intentionally low-order interaction mechanisms compared to dense global coupling (full attention), mirroring the many-body principle of combining local dynamics with restricted interaction structure.
3) **Tensor-network parameterization (MPS/MPO).** The *largest* linear maps in the pipeline—the input projection $\mathbb{R}^K \to \mathbb{R}^D$ and the readout $\mathbb{R}^D \to \mathbb{R}$—are constrained to TT/MPS form (MPO factorization). This imports the key computational idea from many-body simulation; represent large objects through a chain of small cores whose bond

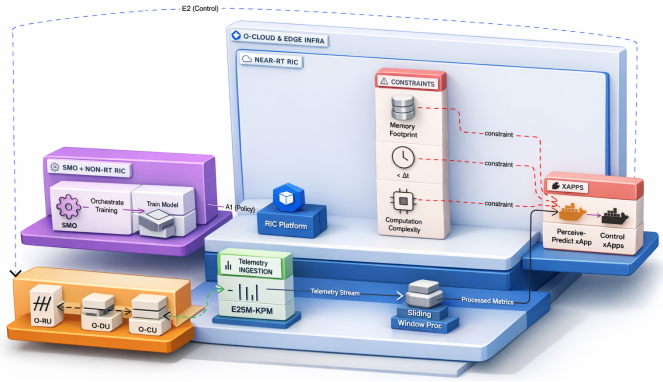

Fig. 1: System model and intelligence placement in the O-RAN architecture. Telemetry collected from E2 nodes (O-CU/O-DU) via the E2 interface using the E2SM-KPM service model is ingested by the Near-RT RIC and processed through sliding-window preprocessing. A perceive–predict xApp operates under Near-RT constraints on memory footprint, computational complexity, and latency ($< \Delta t$), producing short-horizon KPI predictions that drive near-real-time control actions via the E2 control loop. Long-term model training and policy generation are orchestrated by the SMO and Non-RT RIC, with resulting policies/model guidance delivered to the Near-RT RIC over the A1 interface, while trained models are deployed on O-Cloud/edge infrastructure for real-time operation.

dimensions (TT ranks) provide an explicit, interpretable knob for the accuracy–efficiency trade-off.

In summary, the algorithm borrows the *representational mechanism* of quantum many-body methods—low-rank tensor networks with rank-controlled correlation capacity—and combines it with stable linear state-space dynamics for temporal modeling. This yields a structured predictor whose expressivity is tunable (via TT ranks and state dimension) while maintaining deployment-friendly complexity.

III. System Model

A. O-RAN Functional Architecture and Intelligence Placement

We consider the O-RAN Alliance architecture, which decomposes the RAN into interoperable and virtualized components with standardized interfaces [33], [34]. Intelligence is introduced through the RICs, which are logically separated into a Non-Real-Time RIC (Non-RT RIC) and a Near-RT RIC, operating at different control time scales. Figure 1 illustrates the considered O-RAN system model. The Non-RT RIC, hosted within the Service Management and Orchestration (SMO) framework, operates at time scales above one second and is responsible for long-term policy optimization, AI model training, lifecycle management, and enrichment of RAN data. The Near-RT RIC operates at time scales ranging from approximately 10 ms to 1 s and hosts latency-sensitive xApps that perform near-real-time analytics, prediction, and control. These xApps communicate with distributed RAN nodes (e.g., Distributed Unit (O-DU) and Central Unit (O-CU)) via the standardized E2 interface. In this work, we focus on intelligence deployed in the Near-RT RIC, where strict constraints on inference latency, computational complexity, and memory footprint limit the applicability of large-scale deep learning models.

B. O-RAN Telemetry Acquisition via the E2 Interface

The E2 interface provides standardized mechanisms for near-real-time telemetry reporting and control signaling between the Near-RT RIC and RAN nodes. Telemetry is exposed through E2 Service Models (E2SMs), such as E2SM-KPM, which define a structured framework for reporting Key Performance Measurements (KPMs) at configurable periodicities. Let Δt denote the reporting interval configured for an E2SM-KPM subscription. At each reporting instant t, the Near-RT RIC receives KPI measurements aggregated over Δt from one or multiple RAN entities. We model the received telemetry as a discrete-time multivariate signal

$$\mathbf{x}_t = \left[x_t^{(1)}, x_t^{(2)}, \ldots, x_t^{(K)}\right]^\top \in \mathbb{R}^K, \tag{6}$$

where K denotes the number of monitored KPIs. The telemetry stream is noisy and non-stationary due to user mobility, scheduling decisions, interference dynamics, and time-varying traffic.

C. Near-RT Prediction Task Definition

The objective of the perceive–predict xApp is to forecast short-horizon KPI values in order to enable proactive control decisions in the Near-RT RIC. Streaming telemetry received over the E2 interface is first segmented into overlapping sliding windows of fixed lookback length, which serve as strictly causal model inputs. In this work, we focus on *single-step* forecasting ($H = 1$) of a selected target KPI (e.g., RSRP), where the predictor maps each input window to a one-step-ahead estimate. The exact mathematical formulation of the sliding-window construction, causality constraints, and prediction function is given in Section IV-B. The formulation naturally extends to multi-step horizons ($H > 1$) by modifying the output head and training labels, provided that inference latency remains within Near-RT bounds.

D. Latency and Resource Constraints in the Near-RT RIC

The Near-RT RIC is typically deployed on edge cloud infrastructure that is shared with other RAN functions and xApps, which imposes strict operational constraints on any embedded prediction model [35]. In particular, inference must be completed within a small fraction of the control loop interval Δt in order to enable timely decision-making. At the same time, computational cost must scale linearly with the observation window length L and the feature dimensionality to ensure scalability under increasing traffic and monitoring demands. Memory usage is also tightly constrained, requiring both model parameters and intermediate activations to fit within limited budgets available at the edge. Finally, excessive data movement between memory and compute units is undesirable, as virtualization and containerization overheads can significantly amplify memory traffic costs. Collectively, these constraints motivate the use of linear-complexity sequence models with compact

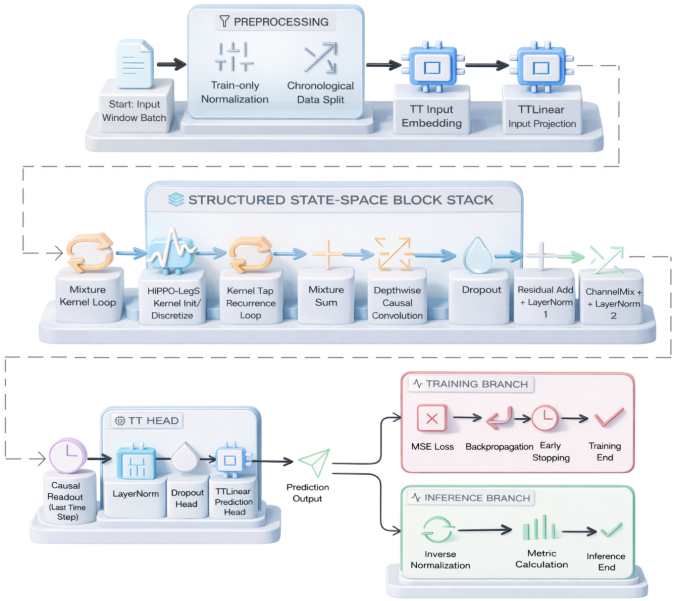

Fig. 2: General end-to-end architecture of the proposed quantum-inspired linear state-space tensor-network forecaster for Near-RT O-RAN telemetry. A chronologically split KPI window is standardized using *train-set* statistics and embedded via a TT/MPS (TTLinear) input projection, then processed by a stack of structured HiPPO–LegS mixture state-space blocks implemented as depthwise causal convolutions with squeeze–excitation gating and gated channel mixing. A causal last-step readout summarizes the sequence, and a TT/MPS prediction head maps this causal summary to the next-step KPI estimate. The *training* elements in the diagram denote the supervision/optimization loop applied to the model output (prediction $\hat{y}$ and ground truth y): parameters (including TT cores and SSM-mixture parameters) are learned by minimizing Mean Squared Error (MSE) $(\hat{y}, y)$ via backpropagation with validation-driven early stopping and best-checkpoint saving. At *inference*, the trained checkpoint is evaluated in a no-gradient forward pass, followed by inverse standardization (and metric computation when evaluating).

parameterizations, rather than quadratic-cost attention-based architectures.

IV. Quantum-Inspired Linear State-Space Tensor Network

Figure 2 summarizes the end-to-end pipeline of the proposed *LiQSS* predictor, from leakage-safe preprocessing to causal readout and deployment-faithful training/inference branches. In particular, the forward path replaces self-attention with structured HiPPO–LegS state-space dynamics realized as mixture-summed kernels and depthwise causal convolutions, while the largest global linear maps (input embedding and prediction head) are parameterized using TT/MPS operators. The complete, code-matched training procedure is given in Algorithm 1 (setup, chronological splits, train-only normalization, and kernel construction) and Algorithm 2 (end-to-end forward pass, optimization, validation, and early stopping). Algorithm 2 is a direct continuation of Algorithm 1: it uses the leakage-safe scalers and the per-block MixtureKernel routine defined in Algorithm 1 to execute the training loop and produce the best checkpoint parameters $\theta^\star$. The corresponding deployment-time inference, including inverse normalization and metric computation, is summarized in Algorithm 3.

A. Motivation and Conceptual Instantiation

Based on the quantum many-body perspective introduced in the Section II, we now clarify how these principles are *instantiated* in the proposed architecture and why they are well aligned with Near-RT O-RAN constraints.

1) From Many-body Structure to Model Design: In quantum many-body systems, complex global behavior emerges from the combination of (i) local dynamics acting on individual degrees of freedom and (ii) restricted interaction operators whose expressive power is controlled by low-rank structure. Our design mirrors this principle at the algorithmic level.

After input embedding, each time step is represented by a latent vector

$$\mathbf{e}_\ell = [e_\ell^{(1)}, \dots, e_\ell^{(D)}]^\top \in \mathbb{R}^D, \tag{7}$$

whose coordinates are treated as distinct degrees of freedom. Temporal evolution is governed by channel-wise SSMs, which act independently on each latent dimension and therefore implement *local* dynamics with linear-time complexity.

2) Controlled Interaction Operators: We introduce cross-channel dependencies through lightweight interaction mechanisms that intentionally avoid dense global coupling. Specifically:

- *Squeeze–excitation gating* performs global but low-rank reweighting of channels based on pooled temporal statistics.
- *Gated channel mixing* introduces pointwise nonlinear coupling across channels without temporal entanglement.

These operators correspond to low-order interaction terms in a many-body system, capturing cross-KPI effects while preserving linear scaling in the window length.

3) Tensor-network Parameterization of Global Maps: The input embedding $\mathbb{R}^K \to \mathbb{R}^D$ and the prediction head $\mathbb{R}^D \to \mathbb{R}$ are implemented using TT/MPS-parameterized linear operators, ensuring that the most expensive global projections in the model respect the same structured, low-coupling design principles as the temporal dynamics.

4) Block-level Composition: Each processing block decomposes the sequence transformation into separable and non-separable components:

$$\mathbf{E} \;\mapsto\; \mathrm{LN}(\mathbf{E} + \mathrm{Mix}(\mathrm{Gate}(\mathrm{SSM}(\mathbf{E})))), \tag{8}$$

where $\mathrm{SSM}(\cdot)$ encodes local temporal evolution, and $\mathrm{Gate}(\cdot)$ and $\mathrm{Mix}(\cdot)$ introduce controlled interactions. This separation is *structural*, not heuristic, and ensures that long-range temporal modeling and cross-channel coupling are achieved without quadratic attention costs.

B. Problem Setup and Notation

Let $\mathbf{x}_t \in \mathbb{R}^K$ denote the vector of K radio KPIs observed at discrete time t. Given a sliding window of fixed length L, the input to the model is $\mathbf{X}_t = [\mathbf{x}_{t-L+1}, \ldots, \mathbf{x}_t] \in \mathbb{R}^{L\times K}$. We consider *single-step forecasting* ($H = 1$) of a target KPI [36], [37], $\hat{y}_{t+1} = f_\theta(\mathbf{X}_t)$, where $f_\theta(\cdot)$ denotes the proposed predictor with parameters θ. For notational convenience, the ℓ-th row of $\mathbf{X}_t$ is denoted by $\mathbf{u}_\ell \in \mathbb{R}^K$ for $\ell = 1, \ldots, L$. Chronological splitting is performed exactly as in Algorithm 1, lines 3–5. Train-only normalization (inputs and target) is performed exactly as in Algorithm 1, lines 6–11, where statistics are computed on training slices only and then applied to all splits.

C. Latent Representation Structure

Each input vector $\mathbf{u}_\ell$ is mapped into a D-dimensional latent representation $\mathbf{e}_\ell$, as introduced in Section IV-A. Latent channels are processed independently by channel-wise temporal dynamics and subsequently coupled through structured interaction operators (gating and mixing described in Section IV-H). The latent tensor $\mathbf{E} \in \mathbb{R}^{|\mathcal{B}|\times L\times D}$ is produced by the TT input projection (Algorithm 2, line 49) and subsequently updated in a block-wise manner by the structured state-space layers (Algorithm 2, lines 50–63).

D. Tensor-Network Linear Operators

The model employs Tensor Train (TT/MPS) parameterizations for selected linear maps, constraining global projections to structured operators while retaining code-level equivalence to dense linear layers at the API level. The TT input projection and TT head are specified in Algorithm 1, lines 13–15, and used in the training forward pass in Algorithm 2, lines 49 and 65, as well as in inference in Algorithm 3, line 5.

E. Input Embedding and Readout

As introduced in Section II-C1, a TT/MPS (or MPO) representation factorizes a large linear operator into a chain of small tensor cores whose bond dimensions control interaction capacity.

1) TT-based Input Embedding: Let $\mathbf{u}_\ell \in \mathbb{R}^K$ denote the vector of KPIs observed at time step ℓ. The input embedding applies a TT-parameterized linear operator, $\mathrm{TTIn} : \mathbb{R}^K \to \mathbb{R}^D$, yielding the latent representation, $\mathbf{e}_\ell = \mathrm{TTIn}(\mathbf{u}_\ell), \ell = 1, \ldots, L$. In our implementation, we choose mode factorizations $\mathbf{n}^{\mathrm{in}} = (1, 1, 13)$ and $\mathbf{m}^{\mathrm{in}} = (4, 4, 4)$ (so that $\prod \mathbf{n}^{\mathrm{in}} = 13$ and $\prod \mathbf{m}^{\mathrm{in}} = 64$), and a TT rank r_{in}, . This performs a structured global projection from KPI space into latent space, coupling inputs through a sequence of low-rank interactions rather than a dense matrix.

2) Causal Readout and TT-based Prediction Head: After processing the embedded sequence through the stacked structured state-space blocks, a causal summary vector is extracted from the final time index, $\mathbf{h}_L = \mathbf{E}_{:,L,:} \in \mathbb{R}^D$. This vector constitutes a sufficient statistic of the past window under the imposed causality constraint. The prediction is obtained by applying layer normalization followed by a TT-parameterized readout operator, $\mathrm{TTHead} : \mathbb{R}^D \to \mathbb{R}$,

$$\hat{y}_{t+1} = \mathrm{TTHead}(\mathrm{LN}(\mathbf{h}_L)) \,. \tag{9}$$

In our implementation, we use $\mathbf{n}^{\mathrm{hd}} = (4, 4, 4)$ and $\mathbf{m}^{\mathrm{hd}} = (1, 1, 1)$ (so that $\prod \mathbf{n}^{\mathrm{hd}} = 64$ and $\prod \mathbf{m}^{\mathrm{hd}} = 1$), and TT rank r_{hd}. As in the input embedding, the TT factorization constrains the global readout map to a low-rank tensor-network structure, ensuring that the final regression step remains parameter-efficient and consistent with the many-body inductive bias of the model.

Algorithm 1 Setup & Kernel

Require: Windows $\{(\mathbf{X}_n, \mathbf{y}_n)\}_{n=1}^N$ with $\mathbf{X}_n \in \mathbb{R}^{L\times K}$, $\mathbf{y}_n \in \mathbb{R}^K$; target index $t^\star$ (RSRP); ratios $\rho_{\mathrm{tr}}, \rho_{\mathrm{va}}$ (chronological slices); batch size B; epochs $E_{\max}$; early-stop patience p; LR η; weight decay λ; grad clip $c_{\max}$=1.0; width D; layers B_ℓ; state dim N_s; mixture comps C_m; dropout p_{do}; HiPPO base init Δt_0; dt growth γ=1.5; TT in-modes $\mathbf{n}^{\mathrm{in}}$, $\mathbf{m}^{\mathrm{in}}$, TT rank r_{in}; TT head modes $\mathbf{n}^{\mathrm{hd}}$, $\mathbf{m}^{\mathrm{hd}}$, TT rank r_{hd}; device.

Ensure: Best params $\theta^\star$, scalers $(\boldsymbol{\mu}_x, \boldsymbol{\sigma}_x), (\mu_y, \sigma_y)$, best val loss $\mathcal{L}^\star_{\mathrm{va}}$.

1: **Harden gradients on.** ▷ matches `torch.set_grad_enabled(True)`
2: Enable global gradients.
3: **Chronological splits (slices).**
4: $n_{\mathrm{tr}} \leftarrow \lfloor \rho_{\mathrm{tr}} N \rfloor$; $n_{\mathrm{va}} \leftarrow \lfloor \rho_{\mathrm{va}} N \rfloor$.
5: $\mathcal{I}_{\mathrm{tr}} \leftarrow \{1{:}n_{\mathrm{tr}}\}$; $\mathcal{I}_{\mathrm{va}} \leftarrow \{n_{\mathrm{tr}}{+}1{:}n_{\mathrm{tr}}{+}n_{\mathrm{va}}\}$; $\mathcal{I}_{\mathrm{te}} \leftarrow \{n_{\mathrm{tr}}{+}n_{\mathrm{va}}{+}1{:}N\}$.
6: **Train-only scalers (leakage-safe; exact).**
7: $\mathcal{X}_{\mathrm{tr}} \leftarrow \{\mathbf{X}_n[\ell, :] \mid n \in \mathcal{I}_{\mathrm{tr}},\ \ell = 1{:}L\}$.
8: $\boldsymbol{\mu}_x \leftarrow \mathrm{mean}(\mathcal{X}_{\mathrm{tr}})$; $\boldsymbol{\sigma}_x \leftarrow \mathrm{std}(\mathcal{X}_{\mathrm{tr}})$; clamp $\boldsymbol{\sigma}_x \geq \epsilon$.
9: $y_n \leftarrow \mathbf{y}_n[t^\star]$ for all n.
10: $\mu_y \leftarrow \mathrm{mean}(\{y_n : n \in \mathcal{I}_{\mathrm{tr}}\})$; $\sigma_y \leftarrow \mathrm{std}(\{y_n : n \in \mathcal{I}_{\mathrm{tr}}\})$; clamp $\sigma_y \geq \epsilon$.
11: Scale all splits:

$$\widetilde{\mathbf{X}}_n = (\mathbf{X}_n - \boldsymbol{\mu}_x) \oslash \boldsymbol{\sigma}_x, \qquad \widetilde{y}_n = (y_n - \mu_y)/\sigma_y.$$

12: **Model (code-exact modules).**
13: **TT input projection** $\mathrm{TTIn} : \mathbb{R}^K \to \mathbb{R}^D$ using TTLinear(in-modes $\mathbf{n}^{\mathrm{in}}$, out-modes $\mathbf{m}^{\mathrm{in}}$, rank r_{in}, bias).
14: **structured state-space Blocks** $\{\mathcal{B}^{(b)}\}_{b=1}^{B_\ell}$. Each block has mixture-kernel + depthwise causal conv + SE gate + dropout + LN + ChannelMix + LN.
15: **TT head** $\mathrm{TTHead} : \mathbb{R}^D \to \mathbb{R}$ using LayerNorm+Dropout+TTLinear(in-modes $\mathbf{n}^{\mathrm{hd}}$, out-modes $\mathbf{m}^{\mathrm{hd}}$, rank r_{hd}).
16: **HiPPO–LegS fixed generator** (stored as buffer per component, numerically identical): build $A_{\mathrm{ct}} \in \mathbb{R}^{N_s\times N_s}$, and reference $B_{\mathrm{ref}} \in \mathbb{R}^{N_s}$.
17: **function** MixtureKernel(b) ▷ returns $K^{(b)} \in \mathbb{R}^{D\times 1\times L}$
18: $K^{(b)} \leftarrow \mathbf{0} \in \mathbb{R}^{D\times 1\times L}$.
19: **for** $m = 1{:}C_m$ **do** ▷ each component is a HiPPOLegSKernel
20: **Component params (learned in code):** $B^{(b,m)} \in \mathbb{R}^{D\times N_s}$, $C^{(b,m)} \in \mathbb{R}^{D\times N_s}$, $D^{(b,m)} \in \mathbb{R}^D$, $\log \Delta t^{(b,m)}$.
21: Init rule (code): $\Delta t^{(b,m)}_{\mathrm{init}} = \Delta t_0 \cdot \gamma^{(m-1)}$, stored via $\log \Delta t$.
22: $\Delta t \leftarrow \mathrm{softplus}(\log \Delta t^{(b,m)}) + 10^{-6}$.
23: $I \leftarrow \mathrm{Id}_{N_s}$; $\mathrm{lhs} \leftarrow I - \frac{1}{2}\Delta t A_{\mathrm{ct}}$; $\mathrm{rhs} \leftarrow I + \frac{1}{2}\Delta t A_{\mathrm{ct}}$.
24: $\bar{A} \leftarrow \mathrm{solve}(\mathrm{lhs}, \mathrm{rhs})$.
25: $\bar{B} \leftarrow \mathrm{solve}(\mathrm{lhs}, \Delta t \cdot B^{(b,m)\top})^\top$. ▷ code computes via transpose
26: $\bar{A}_T \leftarrow \bar{A}^\top$.
27: **Recurrence taps (code exact).**
28: $x \leftarrow \bar{B} \in \mathbb{R}^{D\times N_s}$.
29: **for** $\tau = 0{:}L-1$ **do**
30: $k[\tau] \leftarrow \sum_{j=1}^{N_s} C^{(b,m)}[:, j] \odot x[:, j] \in \mathbb{R}^D$.
31: $x \leftarrow x\,\bar{A}_T$.
32: $k[0] \leftarrow k[0] + D^{(b,m)}$.
33: Stack $K^{(b,m)} \in \mathbb{R}^{D\times L}$ from $\{k[\tau]\}_\tau$ and reshape to $K^{(b,m)}[:, 1, :] \in \mathbb{R}^{D\times 1\times L}$.
34: $K^{(b)} \leftarrow K^{(b)} + K^{(b,m)}$. ▷ mixture sum
35: **return** $K^{(b)}$.

F. Local Temporal Dynamics via HiPPO-LegS State-Space Models

Each latent channel evolves according to an independent linear state-space model

$$\mathbf{s}^{(d)}_{\ell+1} = \mathbf{A}\mathbf{s}^{(d)}_\ell + \mathbf{b}^{(d)} e^{(d)}_\ell, \tag{10}$$

$$h^{(d)}_\ell = (\mathbf{c}^{(d)})^\top \mathbf{s}^{(d)}_\ell + d^{(d)} e^{(d)}_\ell, \tag{11}$$

Algorithm 2 Training

36: **Optimizer & scheduler (code exact).**
37: AdamW with LR η and weight decay λ.
38: ReduceLROnPlateau on val loss: factor 0.5, patience 2.
39: AMP autocast + GradScaler enabled iff CUDA.
40: Initialize $\mathcal{L}_{\text{va}}^{\star} \leftarrow +\infty$; remaining patience $\pi \leftarrow p$; store checkpoint path.
41: **for** $e = 1{:}E_{\max}$ **do**
42: **Train mode.** model $\leftarrow$ `train`.
43: **Training batches shuffled** (DataLoader `shuffle=True`).
44: $\text{sum}_{\text{tr}} \leftarrow 0$; $n_{\text{tr}} \leftarrow 0$.
45: **Ensure grads on in loop** (`with torch.enable_grad():`).
46: **for** mini-batch $(\widetilde{\mathbf{X}}_{\mathcal{B}}, \widetilde{\mathbf{y}}_{\mathcal{B}})$ from train loader **do**
47: Move batch to device. Zero gradients (`set_to_none=True`).
48: **Forward (vectorized; code exact).**
49: $\mathbf{E} \leftarrow \text{TTIn}(\widetilde{\mathbf{X}}_{\mathcal{B}}) \in \mathbb{R}^{|\mathcal{B}| \times L \times D}$.
50: **for** $b = 1{:}B_{\ell}$ **do**
51: $K^{(b)} \leftarrow$ MixtureKernel(b) ▷ $D \times 1 \times L$
52: **Depthwise causal conv (code exact):**
53: $X_{dw} \leftarrow \mathbf{E}^{\top} \in \mathbb{R}^{|\mathcal{B}| \times D \times L}$ (transpose time/channel).
54: $Y_{dw} \leftarrow \text{conv1d}(\text{pad_left}(X_{dw}, L-1), K^{(b)}, \text{groups} = D)$.
55: $\mathbf{Y} \leftarrow Y_{dw}^{\top} \in \mathbb{R}^{|\mathcal{B}| \times L \times D}$.
56: **SE gate (code exact):** pool over time then MLP sigmoid $\Rightarrow$ channel gains; $\mathbf{Y} \leftarrow \mathbf{Y} \odot \mathbf{g}$.
57: **Dropout:** $\mathbf{Y} \leftarrow \text{Drop}(\mathbf{Y})$.
58: **Residual + LN1:** $\mathbf{Y} \leftarrow \text{LN}_1(\mathbf{E} + \mathbf{Y})$.
59: **ChannelMix (code exact: internal residual+LN).**
60: $U \leftarrow W_{\uparrow}\mathbf{Y}$; split $U = (\mathbf{a}, \mathbf{g})$ along channels.
61: $\text{MLPout} \leftarrow W_{\downarrow}(\text{GELU}(\mathbf{a}) \odot \sigma(\mathbf{g}))$.
62: $\mathbf{Z} \leftarrow \text{LN}(\mathbf{Y} + \text{Drop}(\text{MLPout}))$. ▷ ChannelMix returns this
63: **Extra residual + LN2 (code exact):** $\mathbf{E} \leftarrow \text{LN}_2(\mathbf{Y} + \mathbf{Z})$.
64: **Causal readout:** $\mathbf{h} \leftarrow \mathbf{E}[:, L, :]$ (last time index).
65: **TT head (code exact):** $\hat{\mathbf{y}} \leftarrow \text{TTHead}(\mathbf{h}) \in \mathbb{R}^{|\mathcal{B}| \times 1}$.
66: **Loss (scaled space):** $\mathcal{L}_{\mathcal{B}} \leftarrow \text{MSE}(\hat{\mathbf{y}}, \widetilde{\mathbf{y}}_{\mathcal{B}})$.
67: **Backward/update (AMP exact).**
68: Scale loss; backprop; clip $\|\nabla\theta\| \leq c_{\max}$; scaler step(AdamW); scaler update.
69: $\text{sum}_{\text{tr}} \mathrel{+}= \mathcal{L}_{\mathcal{B}} \cdot |\mathcal{B}|$; $n_{\text{tr}} \mathrel{+}= |\mathcal{B}|$.
70: $\mathcal{L}_{\text{tr}} \leftarrow \text{sum}_{\text{tr}} / \max(1, n_{\text{tr}})$.
71: **Validation mode.** model $\leftarrow$ `eval`.
72: $\text{sum}_{\text{va}} \leftarrow 0$; $n_{\text{va}} \leftarrow 0$.
73: Disable grads (`with torch.no_grad():`).
74: **for** mini-batch $(\widetilde{\mathbf{X}}_{\mathcal{B}}, \widetilde{\mathbf{y}}_{\mathcal{B}})$ from val loader **do**
75: $\hat{\mathbf{y}} \leftarrow f_{\theta}(\widetilde{\mathbf{X}}_{\mathcal{B}})$ (same forward).
76: $\mathcal{L}_{\mathcal{B}} \leftarrow \text{MSE}(\hat{\mathbf{y}}, \widetilde{\mathbf{y}}_{\mathcal{B}})$.
77: $\text{sum}_{\text{va}} \mathrel{+}= \mathcal{L}_{\mathcal{B}} \cdot |\mathcal{B}|$; $n_{\text{va}} \mathrel{+}= |\mathcal{B}|$.
78: $\mathcal{L}_{\text{va}} \leftarrow \text{sum}_{\text{va}} / \max(1, n_{\text{va}})$.
79: Scheduler step on $\mathcal{L}_{\text{va}}$.
80: **if** $\mathcal{L}_{\text{va}} < \mathcal{L}_{\text{va}}^{\star} - 10^{-6}$ **then**
81: $\mathcal{L}_{\text{va}}^{\star} \leftarrow \mathcal{L}_{\text{va}}$.
82: Save checkpoint $\theta^{\star} \leftarrow \theta$.
83: $\pi \leftarrow p$.
84: **else**
85: $\pi \leftarrow \pi - 1$.
86: **if** $\pi = 0$ **then**
87: **break**.
88: **Return** $\theta^{\star}$, $(\boldsymbol{\mu}_x, \boldsymbol{\sigma}_x)$, (μ_y, σ_y), $\mathcal{L}_{\text{va}}^{\star}$.

where $\mathbf{A} \in \mathbb{R}^{N_s \times N_s}$ is shared across channels, while $\mathbf{b}^{(d)}, \mathbf{c}^{(d)}, d^{(d)}$ are learned per-channel parameters.

1) HiPPO-LegS Parameterization: The continuous-time generator $\mathbf{A}_{\text{ct}}$ is defined by the HiPPO-LegS [21] operator. A stable discrete-time transition matrix is obtained via bilinear (Tustin) discretization [38]

$$\mathbf{A} = \left(\mathbf{I} - \frac{\Delta t}{2}\mathbf{A}_{\text{ct}}\right)^{-1} \left(\mathbf{I} + \frac{\Delta t}{2}\mathbf{A}_{\text{ct}}\right). \tag{12}$$

2) Convolutional Form: The resulting system admits a causal convolution representation

$$h_{\ell}^{(d)} = \sum_{\tau=0}^{\ell-1} (\mathbf{c}^{(d)})^{\top} \mathbf{A}^{\tau} \mathbf{b}^{(d)} \, e_{\ell-\tau}^{(d)}. \tag{13}$$

The HiPPO-LegS fixed generator $(A_{\text{ct}}, B_{\text{ref}})$ is constructed as in Algorithm 1, line 16. The bilinear discretization is performed as in Algorithm 1, lines 22–25. Kernel tap generation

Algorithm 3 Inference

Require: Best params $\theta^{\star}$; scalers $(\boldsymbol{\mu}_x, \boldsymbol{\sigma}_x)$ and (μ_y, σ_y); test loader providing scaled $(\widetilde{\mathbf{X}}_{\mathcal{B}}, \widetilde{\mathbf{y}}_{\mathcal{B}})$.
Ensure: Predictions $\hat{y}$; MSE, RMSE, MAE in original units.
1: Load $\theta^{\star}$; set model to `eval`.
2: $\text{SSE} \leftarrow 0$, $\text{SAE} \leftarrow 0$, $M \leftarrow 0$.
3: Disable grads (`with torch.no_grad():`).
4: **for** mini-batch $(\widetilde{\mathbf{X}}_{\mathcal{B}}, \widetilde{\mathbf{y}}_{\mathcal{B}})$ from test loader **do**
5: **Forward (in scaled space).** $\widetilde{\hat{\mathbf{y}}} \leftarrow f_{\theta^{\star}}(\widetilde{\mathbf{X}}_{\mathcal{B}})$.
6: **Inverse-scale (code exact).**
7: $\hat{\mathbf{y}} \leftarrow \sigma_y \widetilde{\hat{\mathbf{y}}} + \mu_y$.
8: $\mathbf{y}^{\text{orig}} \leftarrow \sigma_y \widetilde{\mathbf{y}}_{\mathcal{B}} + \mu_y$ ▷ since loader stores scaled targets
9: $\text{SSE} \mathrel{+}= \sum(\hat{\mathbf{y}} - \mathbf{y}^{\text{orig}})^2$; $\text{SAE} \mathrel{+}= \sum|\hat{\mathbf{y}} - \mathbf{y}^{\text{orig}}|$.
10: $M \mathrel{+}=$ number of scalar elements in $\hat{\mathbf{y}}$.
11: $\text{MSE} \leftarrow \text{SSE}/\max(1, M)$; $\text{RMSE} \leftarrow \sqrt{\text{MSE}}$; $\text{MAE} \leftarrow \text{SAE}/\max(1, M)$.
12: **return** predictions and metrics.

via the state recurrence is performed as in Algorithm 1, lines 27–33. The resulting kernel is then applied by depthwise causal convolution in Algorithm 2, lines 52–55.

G. Mixture of HiPPO-LegS Kernels

To increase expressivity while preserving linear complexity, each block employs a mixture of C_m state-space kernels, $\mathbf{K} = \sum_{m=1}^{C_m} \mathbf{K}^{(m)}$. Each component corresponds to an independent HiPPO-LegS parameterization with its own learned (B, C, D) and time scale Δt. Mixture construction is defined by the loop over components (Algorithm 1, lines 19–35), including component initialization (line 21), discretization (lines 22–25), recurrence (lines 27–33), and mixture summation (line 34). Kernel creation is invoked per block during training (Algorithm 2, line 51).

H. Channel Gating and Mixing

After the depthwise causal state-space convolution, each block produces an intermediate latent sequence $\mathbf{Y} \in \mathbb{R}^{B \times L \times D}$, where B is the batch size, L the window length, and D the latent channel width. To capture non-stationary cross-channel (cross-KPI) dependencies without self-attention, we apply two lightweight interaction operators: (i) squeeze–excitation (SE) channel gating, and (ii) token-wise gated channel mixing. Both operators preserve linear scaling in L and are composed using residual connections and layer normalization.

1) Squeeze–excitation channel gating: SE gating introduces global, window-level channel reweighting based on aggregated temporal statistics. First, a per-channel summary is obtained by averaging over the temporal dimension

$$\mathbf{s} \;=\; \frac{1}{L}\sum_{\ell=1}^{L} \mathbf{Y}_{:,\ell,:} \in \mathbb{R}^{B \times D}. \tag{14}$$

This summary is mapped to channel gains through a low-rank gating operator

$$\mathbf{g} \;=\; \sigma(\phi(\mathbf{s}W_1 + \mathbf{b}_1)\, W_2 + \mathbf{b}_2) \in (0,1)^{B \times D}, \tag{15}$$

where $\phi(\cdot)$ is a pointwise nonlinearity, $\sigma(\cdot)$ is the sigmoid function, $W_1 \in \mathbb{R}^{D \times D_r}$, $W_2 \in \mathbb{R}^{D_r \times D}$, and $D_r = \max(1, \lfloor D/r \rfloor)$ is a reduction dimension. The gated sequence is then obtained by channel-wise modulation

$$\widetilde{\mathbf{Y}}_{:,\ell,:} \;=\; \mathbf{Y}_{:,\ell,:} \odot \mathbf{g}, \qquad \ell = 1, \ldots, L, \tag{16}$$

where $\odot$ denotes elementwise multiplication with broadcasting over time. SE gating acts as a structured global interaction operator, adaptively emphasizing informative channels based on the current temporal context while avoiding quadratic-time attention.

2) Token-wise gated channel mixing: To introduce nonlinear cross-channel interactions at each time step without mixing information across time, we apply a gated channel-mixing operator independently at each temporal index. Let $\mathbf{u}_\ell \in \mathbb{R}^{B\times D}$ denote the input at time step ℓ. First, an expansion and split operation produces content and gate components

$$\big[\mathbf{a}_\ell, \mathbf{q}_\ell\big] = \mathbf{u}_\ell W_\uparrow + \mathbf{b}_\uparrow, \qquad \mathbf{a}_\ell, \mathbf{q}_\ell \in \mathbb{R}^{B\times D_m}, \tag{17}$$

where $W_\uparrow \in \mathbb{R}^{D\times 2D_m}$ and $D_m = \alpha D$ is an expansion dimension. The mixed output is then formed by gated nonlinear interaction followed by dimensionality reduction

$$\mathrm{Mix}(\mathbf{u}_\ell) = \Big(\phi(\mathbf{a}_\ell) \odot \sigma(\mathbf{q}_\ell)\Big) W_\downarrow + \mathbf{b}_\downarrow, \qquad W_\downarrow \in \mathbb{R}^{D_m\times D}. \tag{18}$$

This operator couples channels within each time step while preserving temporal independence across ℓ.

3) Residual composition at the block level: Let $\mathbf{E} \in \mathbb{R}^{B\times L\times D}$ denote the input to a block, and $\mathbf{Y} = \mathrm{SSM}(\mathbf{E})$ the output of the structured state-space operator. The block output is formed through the following sequence of residual compositions

$$\mathbf{Y}_1 = \mathrm{LN}_1\Big(\mathbf{E} + \mathrm{Drop}\big(\mathrm{SE}(\mathbf{Y})\big)\Big), \tag{19}$$

$$\mathbf{Z} = \mathrm{LN}_m\Big(\mathbf{Y}_1 + \mathrm{Drop}\big(\mathrm{Mix}(\mathbf{Y}_1)\big)\Big), \tag{20}$$

$$\mathbf{E}^+ = \mathrm{LN}_2\Big(\mathbf{Y}_1 + \mathbf{Z}\Big). \tag{21}$$

The first residual path injects temporally filtered features into the block input. The second applies gated channel mixing with normalization. The final outer residual introduces an additional skip connection around the entire interaction sublayer, improving optimization stability and enabling deep stacking of blocks. Together, these operations provide controlled cross-channel interaction while maintaining linear-time temporal modeling and strict causality.

I. End-to-End Forward Map

For a mini-batch in scaled space, the forward pass proceeds as follows:

1) **TT input embedding:** $\mathbf{E} \leftarrow \mathrm{TTIn}(\widetilde{\mathbf{X}}_{\mathcal{B}})$.
2) **Block stack:** for $b = 1{:}B_\ell$, construct $K^{(b)}$ and apply depthwise causal convolution, gating, and channel mixing.
3) **Causal readout:** $\mathbf{h} \leftarrow \mathbf{E}[:, L, :]$ (last time index).
4) **TT head:** $\hat{\mathbf{y}} \leftarrow \mathrm{TTHead}(\mathbf{h})$.

These steps correspond exactly to Algorithm 2, lines 49–65, with kernel construction at line 51 and depthwise causal convolution at lines 52–55.

J. Training and Inference

The model is trained using mean-squared error in normalized space and optimized with AdamW, a validation-driven learning-rate scheduler, mixed precision when available, gradient clipping, and early stopping. Optimizer, scheduler, and Automatic Mixed Precision (AMP) configuration follow Algorithm 2, lines 36–40. The training loop (including device transfer, zeroing gradients, forward, loss, backward, clipping, and update) follows lines 41–69. Validation follows lines 71–79, and early stopping/checkpointing follows lines 80–87, returning the best checkpoint at line 88. Inference initialization follows Algorithm 3, lines 1–3. Forward prediction in scaled space is performed at line 5. Inverse-scaling is performed at lines 7–8, error accumulation at line 9–10, metric computation at line 11, and return at line 12.

K. Computational Complexity

We analyze the computational and memory complexity of the proposed LiQSS architecture and compare it with standard Transformer self-attention. The analysis is expressed in terms of the window length L, latent width D, state dimension N_s, and number of stacked blocks B_ℓ. Each structured state-space block performs channel-wise temporal modeling via causal depthwise convolutions, followed by lightweight interaction operators (squeeze–excitation gating and gated channel mixing). For a single block, the dominant cost arises from state-space kernel evaluation and token-wise channel mixing. Aggregating over B_ℓ blocks, the per-window computational complexity is $\mathcal{O}(B_\ell\, L\, D\, N_s)$, which scales linearly with the sequence length L and contains no quadratic terms. Activation memory likewise scales linearly in L, with an additional $\mathcal{O}(DN_s)$ contribution from state buffers. By construction, the model avoids attention matrices entirely, eliminating the $\mathcal{O}(L^2)$ [39] compute and memory overhead associated with full self-attention. Furthermore, Tensor Train (TT/MPS) parameterization of the input projection and prediction head substantially reduces parameter count and memory traffic for global linear maps without altering asymptotic runtime complexity. To facilitate comparison, consider a sequence model with input length L and latent width D. Suppose that: (i) a Transformer layer employs full self-attention with H_a heads and per-head dimension d_h (so $D = H_a d_h$), and (ii) the proposed model uses channel-wise state-space dynamics with state dimension N_s and a gated channel-mixing layer of width $D_m = \alpha D$, $\alpha \geq 1$. Ignoring constant factors and bias terms, the per-layer complexity is summarized below.

1) **Transformer (full self-attention), per layer:**

$$\begin{aligned} \text{time} &= \mathcal{O}\big(LD^2 + L^2 D\big)\,, \\ \text{activation memory} &= \mathcal{O}\big(L^2\big)\,. \end{aligned}$$

2) **Proposed SSM + TT block, per layer:**

$$\begin{aligned} \text{time} &= \mathcal{O}(LDN_s + LDD_m)\,, \\ \text{activation memory} &= \mathcal{O}(LD + DN_s)\,. \end{aligned}$$

For sufficiently large L and fixed D and N_s, Transformer layers exhibit quadratic scaling in L, whereas the proposed architecture scales linearly. Here, *time complexity* refers to asymptotic operation count and is hardware-agnostic, while

activation memory denotes runtime storage of intermediate tensors during forward and backward passes.

V. Experimental Setup

A. Data Collection and KPIs

The end-to-end telemetry acquisition pipeline and the associated implementation details follow the same procedure established in our earlier studies [40], [41]. In brief, KPIs are collected from an O-RAN test environment and curated into a forecasting-ready dataset under a consistent preprocessing and quality-control workflow. To facilitate reproducibility and encourage further investigation, we release the dataset publicly[2]. We consider $K = 13$ KPIs extracted from the E2 Service Model for E2SM-KPM reports: Modulation and Coding Scheme (MCS), Channel Quality Indicator (CQI), Rank Indicator (RI), Precoding Matrix Indicator (PMI), Buffer occupancy (Buffer), Physical Resource Blocks (PRBs), Reference Signal Received Quality (RSRQ), RSRP, Received Signal Strength Indicator (RSSI), SINR, Spectral Efficiency, Block Error Rate (BLER), and Delay. The primary forecasting task in this paper is next-step prediction of *RSRP* (target index $t^\star$), a representative radio-quality KPI widely used for mobility management and link-adaptation decisions.

B. Baselines

To ensure a fair and representative evaluation, we compare the proposed LiQSS model against a diverse set of state-of-the-art baselines spanning Transformer-based architectures, attention-efficient variants, foundation-style time-series models, and structured state-space models. All selected baselines are widely used in the time-series literature or have been recently proposed for long-sequence modeling, and collectively reflect the design space summarized in Table I of Section I-A. All baselines are evaluated under the same experimental protocol: chronological data splits, train-only normalization, strictly causal inference, and identical evaluation metrics. Inference latency is measured on GPU using synchronized CUDA events [42], [43], ensuring fair comparison of deployment-relevant performance. For a fair comparison under identical time and memory constraints, we standardize the data pipeline and training procedure across all models. We also use compact baseline versions that retain each method's key inductive bias. These implementations are not faithful re-runs of the original codebases; they are designed for consistency and comparability rather than exact replication.

C. Model Hyperparameters

All experiments use a fixed, code-faithful hyperparameter configuration summarized in Table III (notations follow Table II). Beyond these hyperparameters, experiments use chronological data splitting with the remaining 15% reserved for testing, normalize features using training-set statistics only, include bias terms in both TT operators, learn $\Delta t^{(b,m)}$ with a softplus positivity constraint while keeping the continuous-time generator fixed, use a fixed random seed of 42, and run on a single CUDA-enabled NVIDIA T4 GPU.

[2]A curated release is hosted on IEEE DataPort: https://ieee-dataport.org/documents/video-streaming-network-kpis-o-ran-testing

TABLE III: LiQSS Model Hyperparameter Configuration.

Symbol	Description	Value
Input, windows, and dimensions		
K	Number of monitored KPIs	13
L	Lookback window length	32
H	Forecast horizon	1
D	Latent channel width	64
B_ℓ	Number of stacked SSM blocks	2
N_s	Per-channel SSM state dimension	32
C_m	HiPPO–LegS mixture components per block	2
α	ChannelMix expansion factor	1
D_m	ChannelMix hidden width ($D_m = \alpha D$)	64
Regularization and gating		
p_{do}	Dropout probability	0.1
HiPPO–LegS discretization		
Δt_0	Base time-step initialization	0.1
γ	Geometric growth factor	1.5
$\Delta t^{(b,m)}$	Learned positive step size	learned
TT/MPS parameterization		
$\mathbf{n}^{\mathrm{in}}$	TT input mode factorization	$(1, 1, 13)$
$\mathbf{m}^{\mathrm{in}}$	TT input output modes	$(4, 4, 4)$
r_{in}	TT rank (input projection)	4
$\mathbf{n}^{\mathrm{hd}}$	TT head input modes	$(4, 4, 4)$
$\mathbf{m}^{\mathrm{hd}}$	TT head output modes	$(1, 1, 1)$
r_{hd}	TT rank (prediction head)	4
Optimization and training		
η	Learning rate (AdamW)	3×10^{-3}
λ	Weight decay (AdamW)	10^{-4}
$c_{\max}$	Gradient clipping threshold	1.0
$E_{\max}$	Maximum training epochs	120
p	Early-stopping patience	30
B	Batch size	256
ρ_{tr}	Training split ratio	0.70
ρ_{va}	Validation split ratio	0.15

VI. Performance and Numerical Results

A. Benchmark Results and Overall Comparison

1) Accuracy—Control-grade Prediction with Competitive Error: As shown in Table IV, LiQSS attains Root Mean Squared Error (RMSE) = 0.2866, MAE = 0.1641, and MSE = 0.0821 on next-step RSRP forecasting. Among the SSM family, LiQSS improves upon the strongest SSM baselines:

- **vs. WM–MS^{3}M:** RMSE improves by $\approx 1.74\%$, Mean Absolute Error (MAE) by $\approx 1.99\%$, and MSE by $\approx 3.46\%$.
- **vs. MS^{3}M:** RMSE improves by $\approx 1.78\%$, MAE by $\approx 3.65\%$, and MSE by $\approx 3.54\%$.

This indicates that the proposed *HiPPO–LegS mixture dynamics* plus *quantum-inspired tensor-network parameterization* provides a measurable gain beyond prior structured-SSM forecasters, despite operating under the same strictly causal and leakage-safe evaluation pipeline.

Across Transformer-based methods, LiQSS remains strongly competitive and typically superior. For example, compared to Chronos-GPT, LiQSS reduces RMSE by $\approx 35.67\%$ and MAE by $\approx 10.37\%$. Methods such as RWKV, Performers, RetNet, PatchTST, and iTransformer exhibit substantially larger errors in this setting, suggesting that attention/Transformer capacity does not automatically translate to control-grade accuracy under Near-RT constraints and this specific O-RAN telemetry regime.

Crossformer attains RMSE $= 0.295324$ in Table IV, which is slightly higher than LiQSS (RMSE $= 0.286599$), i.e., $\approx 3.05\%$ worse in RMSE. However, this comes with *much higher* deployment cost; Crossformer is $\approx 36\times$ larger in parameters and $\approx 2.96\times$ slower in inference than LiQSS

TABLE IV: Benchmark Results Comparing the Proposed LiQSS with SSM- and Transformer-Based Baselines.

Model	RMSE	MAE	MSE	Skill (R)	Skill (M)	R^2	#Params	Infer (s)
Proposed Method								
LiQSS	0.286599	0.164083	0.082139	0.919865	0.939650	0.993276	44,109	0.000456
SSM-based Methods								
WM–MS^{3}M [12]	0.291687	0.167417	0.085081	0.918448	0.938430	0.993035	477,802	0.000647
MS^{3}M [11]	0.291806	0.170298	0.085151	0.918414	0.937370	0.993030	698,449	0.000643
Transformer-based Methods								
RWKV [8]	1.480259	0.407525	2.191166	0.576394	0.848496	0.812361	26,269,696	0.002103
Performers [20]	0.786704	0.276759	0.618902	0.774869	0.897110	0.947001	14,156,160	0.002634
RetNet [9]	0.598374	0.208329	0.358051	0.828763	0.922550	0.969338	18,930,432	0.001522
Chronos-T5 [10]	2.518750	1.673298	6.344100	0.279208	0.377925	0.456727	14,209,536	0.000790
Chronos-GPT [10]	0.445510	0.183071	0.198479	0.872508	0.931941	0.983003	6,840,320	0.000749
PatchTST [6]	3.257556	2.539881	10.611672	0.089299	0.066044	0.131326	662,403	0.001148
iTransformer [19]	3.305829	2.614187	10.928505	0.075758	0.038648	0.105390	814,273	0.001347
FEDformer [4]	0.598971	0.393850	0.358766	0.832540	0.855164	0.970631	756,569	0.001120
Informer [3]	0.367830	0.193562	0.135299	0.897161	0.928818	0.988924	1,256,449	0.001365
TFT [44]	0.421653	0.240557	0.177791	0.882113	0.911535	0.985446	2,510,702	0.001377
ETSformer [5]	0.333457	0.230507	0.111193	0.906772	0.915231	0.990898	800,376	0.001143
Crossformer [7]	0.295324	0.175972	0.087842	0.913117	0.932184	0.991612	1,591,321	0.001349

Notes: Inference timing on GPU was measured using synchronized CUDA events [42], [43].

(see Section VI-A3). Therefore, LiQSS provides the best *accuracy–efficiency* trade-off and dominates the practical Near-RT operating point.

2) Forecast Skill and Goodness-of-Fit: Beyond absolute error metrics (RMSE/MAE/MSE), Table IV reports *forecast skill scores* that quantify relative performance against simple, deployment-relevant reference predictors. Relative evaluation against such benchmarks is standard practice in the forecasting literature, particularly when assessing practical predictive utility beyond naive baselines [45].

Let $\mathcal{E}(\hat{y}, y)$ denote the mean-squared error (MSE) over the evaluation set $\mathcal{E}(\hat{y}, y) = \frac{1}{|\mathcal{D}|}\sum_{t\in\mathcal{D}}\big(\hat{y}_{t+1} - y_{t+1}\big)^2$, and let $\hat{y}_{t+1}^{\text{model}}$ be the one-step-ahead forecast produced by the model.

a) Skill(R)—Persistence Skill: The persistence (random-walk) baseline assumes that the next value equals the most recently observed value $\hat{y}_{t+1}^{(R)} = y_t$. The corresponding skill score is defined as, $\text{Skill}(R) = 1 - \frac{\mathcal{E}(\hat{y}_{t+1}^{\text{model}}, y_{t+1})}{\mathcal{E}(\hat{y}_{t+1}^{(R)}, y_{t+1})}$, following the standard MSE-based skill-score formulation [46]. Thus, $\text{Skill}(R) = 1$ indicates perfect forecasting, $\text{Skill}(R) = 0$ indicates parity with persistence, and $\text{Skill}(R) < 0$ indicates worse-than-persistence performance. For short-horizon time-series forecasting, persistence is a strong and highly relevant baseline [45].

b) Skill(M)—Mean Skill: The mean baseline predicts a constant value equal to the training-set mean $\hat{y}_{t+1}^{(M)} = \mu_{\text{tr}}$. The associated skill score is $\text{Skill}(M) = 1 - \frac{\mathcal{E}(\hat{y}_{t+1}^{\text{model}}, y_{t+1})}{\mathcal{E}(\hat{y}_{t+1}^{(M)}, y_{t+1})}$, which quantifies improvement over a stationary reference predictor using the same skill-score normalization [46].

c) LiQSS Model: Using MSE-based skill scores on the test set, LiQSS achieves $\text{Skill}(R) = 0.9199$ and $\text{Skill}(M) = 0.9397$, indicating that its test MSE is reduced to 8.01% of the persistence baseline and 6.03% of the mean baseline, respectively. Together with a high coefficient of determination ($R^2 = 0.9933$, test set), these results demonstrate that LiQSS accurately captures both short-horizon dynamics (beating the strong persistence reference) and the overall variance structure (beating the mean reference), while preserving strict causality and linear-time execution.

3) Efficiency—Parameter count, Latency, and Near-RT Suitability: The most deployment-relevant outcome is that LiQSS achieves high accuracy at a tiny cost of *44,109 parameters* and $0.000\,456\,\text{s}$ inference time per window on the target GPU. This yields:

- **vs. WM–MS^{3}M:** $\approx 90.77\%$ fewer parameters (about $10.8\times$ smaller) and $\approx 1.42\times$ faster inference.
- **vs. MS^{3}M:** $\approx 93.69\%$ fewer parameters (about $15.8\times$ smaller) and $\approx 1.41\times$ faster inference.
- **vs. Crossformer:** $\approx 97.23\%$ fewer parameters (about $36\times$ smaller) and $\approx 2.96\times$ faster inference.
- **vs. Chronos-GPT:** $\approx 99.36\%$ fewer parameters (about $155\times$ smaller) and $\approx 1.64\times$ faster inference.

These gains directly support Near-RT RIC operation where model size, memory traffic, and tail latency often dominate end-to-end xApp responsiveness.

B. Qualitative KPI Prediction and Temporal Fidelity

Figure 3 illustrates qualitative one-step-ahead forecasting performance across seven representative KPIs, comparing ground truth telemetry against the model's predictions over the final 700 test samples. Across radio-quality indicators (RSRP, RSRQ, and SINR), the model closely tracks both slow-varying trends and short-term fluctuations, with small residual errors except at abrupt regime transitions. This indicates that the state-space backbone captures dominant channel dynamics without relying on future information. For control-related and load-sensitive KPIs (PRBs and SE), predictions remain well aligned with ground truth, including sharp drops and bursts that reflect scheduler-driven behavior. This is particularly important because PRBs act as explicit control inputs during planning, and accurate reconstruction confirms internal consistency between action channels and predicted network responses. Discrete or quasi-discrete indicators (CQI and RI) exhibit piecewise-constant behavior with occasional jumps. The model successfully anticipates most transitions, while minor misalignments

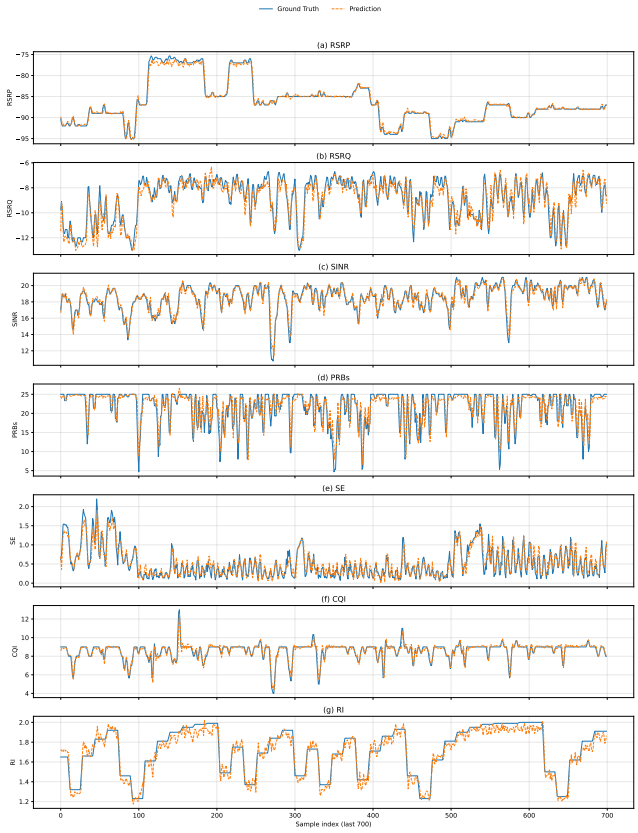

Fig. 3: Ground truth versus one-step-ahead predictions for key O-RAN KPIs over the last 700 test samples.

occur near abrupt state changes—an expected limitation under strictly causal, one-step forecasting. Overall, the figure confirms that the proposed LiQSS model delivers high-fidelity, leakage-safe predictions across heterogeneous KPIs, supporting accurate next-step forecasting for Near-RT O-RAN control.

C. Empirical Evidence of Linear Scaling

Figure 4 empirically demonstrates that LiQSS exhibits linear behavior in practice across training time, inference time, and memory usage as the lookback window length L increases. Figure 4-(a) shows that training time grows approximately proportionally with L, increasing smoothly from 8.67×10^{-5} s at L=8 to 1.68×10^{-4} s at L=32, confirming that backpropagation preserves linear scaling with respect to the lookback window length. Figure 4-(b) confirms the same trend at inference time, where latency increases linearly from 2.34×10^{-5} s to 3.87×10^{-5} s as L quadruples, ruling out hidden quadratic costs during deployment. Figure 4-(c) further shows that peak memory consumption scales linearly with L, growing from 33.26 MB to 77.91 MB, consistent with storing only $\mathcal{O}(LD)$ activations rather than $\mathcal{O}(L^2)$ attention maps. Together, these subplots confirm that the architectural linearity of LiQSS directly translates into real-world execution.

D. Sensitivity Analysis

We analyze how LiQSS changes with three key capacity knobs while keeping the dataset, leakage-safe preprocessing,

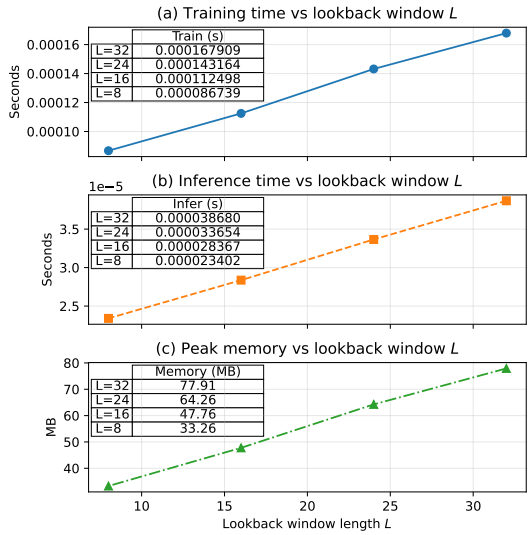

Fig. 4: Empirical evidence of linear-time behavior in LiQSS. Here, training time is the average seconds per example spent on one training step (forward pass + loss + backward pass + optimizer update) measured on a fixed batch after warm-up.

training protocol, and all other hyperparameters fixed: (i) the TT rank r (controls coupling capacity in the TT/MPS input and head), (ii) the number of HiPPO–LegS mixture components per block C_m (controls multi-timescale kernel capacity), and (iii) the SSM state dimension N_s (controls temporal memory per channel). The results in Table V show that performance is generally stable with modest and sometimes non-monotonic trends. Increasing TT rank yields only incremental accuracy gains (best RMSE at r=16) but increases latency, making r=4 the best Near-RT operating point. Increasing mixture components improves slightly up to C_m=4, but larger mixtures ($C_m \geq 6$) degrade accuracy while substantially increasing parameters, indicating diminishing returns/over-parameterization for one-step forecasting. For the SSM state dimension, very small N_s underfits, while overly large N_s increases cost and can hurt accuracy; N_s=32 provides the best overall balance. Overall, the default configuration (r=4, C_m=2, N_s=32) remains the strongest accuracy–efficiency choice for Near-RT deployment, with (r=16, C_m=4, N_s=32) as an accuracy-leaning alternative when latency budget allows.

VII. Conclusion

In this paper, we have proposed *LiQSS*, a post-Transformer, quantum-inspired linear state-space tensor-network architecture for control-grade KPI forecasting in Near-RT O-RAN systems. By replacing quadratic self-attention with stable HiPPO–LegS state-space dynamics implemented via causal depthwise convolutions, and by constraining global linear operators through TT/MPS parameterization, LiQSS achieves strictly linear-time sequence modeling with a compact model footprint. Extensive evaluation on a bespoke O-RAN telemetry dataset comprising 59,441 sliding windows across 13 KPIs has demonstrated that LiQSS delivers forecasting accuracy superior to, state-of-the-art Transformer and structured-SSM baselines, while

TABLE V: Sensitivity Test of LiQSS.

Setting	RMSE	#Params	Infer (s)	R^2
TT rank r ***(with*** C_m=2, N_s=32***)***				
r=2	0.288711	43,885	0.000549	0.993177
r=4	0.286599	44,109	0.000456	0.993276
r=8	0.290643	44,749	0.000584	0.993085
r=16	0.283614	46,797	0.000727	0.993415
Mixture components C_m ***(with*** r=4, N_s=32***)***				
C_m=2	0.286599	44,109	0.000456	0.993276
C_m=4	0.284246	60,753	0.000593	0.993386
C_m=6	0.286833	77,397	0.000656	0.993265
C_m=8	0.291332	94,041	0.000623	0.993052
SSM state dimension N_s ***(with*** r=4, C_m=2***)***				
N_s=8	0.297041	31,821	0.000564	0.992777
N_s=16	0.291094	35,917	0.000462	0.993064
N_s=32	0.286599	44,109	0.000456	0.993276
N_s=64	0.292463	60,493	0.000616	0.992998

reducing trainable parameter count and significantly lowering inference latency. These results support the viability of post-Transformer, state-space, and tensor-network-based models as enabling technologies for deployment-faithful intelligence in future 6G Near-RT RIC environments.

References

[1] Z. Wang *et al.*, "Ultra-Low-Latency Edge Inference for Distributed Sensing," *IEEE Transactions on Wireless Communications*, vol. 25, pp. 1908–1922, 2025.

[2] B. Agarwal *et al.*, "Open RAN for 6G Networks: Architecture, Use Cases and Open Issues," *IEEE Communications Surveys & Tutorials*, vol. 28, pp. 2881–2924, 2025.

[3] H. Zhou *et al.*, "Informer: Beyond Efficient Transformer for Long Sequence Time-Series Forecasting," in *Proceedings of the AAAI Conference on Artificial Intelligence*, vol. 35, no. 12, 2021, pp. 11 106–11 115.

[4] T. Zhou *et al.*, "FEDformer: Frequency Enhanced Decomposed Transformer for Long-term Series Forecasting," in *Proceedings of the 39th International Conference on Machine Learning*, vol. 162. PMLR, 2022.

[5] G. Woo *et al.*, "ETSformer: Exponential Smoothing Transformers for Time-series Forecasting," *arXiv preprint arXiv:2202.01381*, 2022.

[6] Y. Nie *et al.*, "A Time Series is Worth 64 Words: Long-term Forecasting with Transformers," in *The Eleventh International Conference on Learning Representations*, 2023.

[7] Y. Zhang and J. Yan, "Crossformer: Transformer Utilizing Cross-Dimension Dependency for Multivariate Time Series Forecasting," in *The Eleventh International Conference on Learning Representations*, 2023.

[8] B. Peng *et al.*, "RWKV: Reinventing RNNs for the Transformer Era," *arXiv preprint arXiv:2305.13048*, 2023.

[9] Y. Sun *et al.*, "Retentive Network: A Successor to Transformer for Large Language Models," *arXiv preprint arXiv:2307.08621*, 2023.

[10] A. F. Ansari *et al.*, "Chronos: Learning the Language of Time Series," *Transactions on Machine Learning Research*, 2024.

[11] F. Rezazadeh *et al.*, "Rivaling Transformers: Multi-Scale Structured State-Space Mixtures for Agentic 6G O-RAN," *arXiv preprint arXiv:2510.05255*, 2025.

[12] F. Rezazadeh, H. Chergui, M. Debbah, H. Song, D. Niyato, and L. Liu, "Agentic World Modeling for 6G: Near-Real-Time Generative State-Space Reasoning," *arXiv preprint arXiv:2511.02748*, 2025.

[13] J. T. H. Smith *et al.*, "Simplified State Space Layers for Sequence Modeling," in *ICLR*, 2023.

[14] A. Gu *et al.*, "HiPPO: Recurrent Memory with Optimal Polynomial Projections," in *NeurIPS*, 2020.

[15] J. Dborin *et al.*, "Matrix Product State Pre-Training for Quantum Machine Learning," *Quantum Science and Technology*, vol. 7, no. 3, 2022.

[16] S. Glisic and B. Lorenzo, "Quantum computing and neuroscience for 6G/7G networks: Survey," *Intelligent Systems with Applications*, 2024.

[17] H. Tasaki, *Physics and Mathematics of Quantum Many-Body Systems*, 1st ed., ser. Graduate Texts in Physics. Springer Cham, 2020.

[18] T.-D. Bradley *et al.*, "Modeling Sequences with Quantum States: A Look Under the Hood," *ML: Science and Technology*, vol. 1, no. 3, 2020.

[19] Y. Liu *et al.*, "iTransformer: Inverted Transformers Are Effective for Time Series Forecasting," in *The Twelfth ICLR*, 2024.

[20] K. Choromanski *et al.*, "Rethinking Attention with Performers," in *ICLR*, 2021.

[21] A. Gu *et al.*, "How to Train Your HiPPO: State Space Models with Generalized Orthogonal Basis Projections," 2022.

[22] C. Guo *et al.*, "Matrix Product Operators for Sequence-to-Sequence Learning," *Physical Review E*, vol. 98, no. 4, 2018.

[23] J. Ren *et al.*, "Time-dependent Density Matrix Renormalization Group Method for Quantum Dynamics in Complex Systems," *Wiley Interdisciplinary Reviews: Computational Molecular Science*, vol. 12, 2022.

[24] P. Balazs and N. Teofanov, "Continuous Frames in Tensor Product Hilbert Spaces, Localization Operators and Density Operators," *Journal of Physics A: Mathematical and Theoretical*, vol. 55, no. 14, 2022.

[25] F. Bach, "Information Theory With Kernel Methods," *IEEE Transactions on Information Theory*, vol. 69, no. 2, pp. 752–775, Feb. 2023.

[26] J. Illiano *et al.*, "Quantum MAC: Genuine Entanglement Access Control via Many-Body Dicke States," *IEEE Transactions on Communications*, vol. 72, no. 4, pp. 2090–2105, 2024.

[27] S. Cheng *et al.*, "Highly Parallel Singular Value Decomposition for Low-Latency MIMO Processing," in *2025 IEEE Workshop on Signal Processing Systems (SiPS)*, 2025.

[28] M. Kumar, "On Properties of Schmidt Decomposition," *arXiv preprint arXiv.2411.05703*, 2024.

[29] P. Calabrese and J. Cardy, "Entanglement Entropy and Quantum Field Theory," *Journal of Statistical Mechanics: Theory and Experiment*, 2004.

[30] N. Paul, "Area-law Entanglement from Quantum Geometry," *Physical Review B*, vol. 109, 2024.

[31] Y. Qiu *et al.*, "Efficient Tensor Robust PCA Under Hybrid Model of Tucker and Tensor Train," *IEEE Signal Processing Letters*, vol. 29, pp. 627–631, 2022.

[32] A. Novikov *et al.*, "Tensorizing Neural Networks," in *NIPS'15: Proceedings of the 29th International Conference on Neural Information Processing Systems*, 2015, pp. 442–450.

[33] O-RAN Software Community. (2023) O-RAN Architecture Overview. [Online]. Available: https://docs.o-ran-sc.org/en/latest/architecture/architecture.html

[34] ETSI, "ETSI TS 104 040 V4.0.0: Publicly Available Specification (PAS); E2 interface: RAN Function-specific Service Models (O-RAN E2SMs)," European Telecommunications Standards Institute (ETSI), Tech. Rep. TS 104 040 V4.0.0, 2024. [Online]. Available: https://www.etsi.org/deliver/etsi_ts/104000_104099/104040/04.00.00_60/ts_104040v040000p.pdf

[35] G. Matheus Almeida, "RIC-O: Efficient Placement of a Disaggregated and Distributed RAN Intelligent Controller with Dynamic Clustering of Radio Nodes," *IEEE Journal on Selected Areas in Communications*, vol. 42, no. 2, pp. 446–459, 2023.

[36] K. Benidis *et al.*, "Deep Learning for Time Series Forecasting: Tutorial and Survey," *ACM Computing Surveys*, vol. 55, no. 6, pp. 1–36, 2022.

[37] D. Salinas *et al.*, "DeepAR: Probabilistic forecasting with autoregressive recurrent networks," *International Journal of Forecasting*, vol. 36, no. 3, pp. 1181–1191, 2020.

[38] J. P. Hespanha, *Linear Systems Theory*, 2nd ed. Princeton, NJ: Princeton University Press, 2018.

[39] A. Vaswani *et al.*, "Attention Is All You Need," in *Advances in Neural Information Processing Systems (NeurIPS)*, vol. 30, 2017, pp. 5998–6008.

[40] J. Dai, R. Zhao, F. Rezazadeh, L. Zheng, H. Wang, and L. Liu, "Learning Low-Dimensional Representation for O-RAN Testing via Transformer-ESN," 2025, accepted for publication at IEEE MASS, 2025.

[41] F. Rezazadeh *et al.*, "An Experimental Reservoir-Augmented Foundation Model: 6G O-RAN Case Study," 2025, accepted to publish at GACLM 2025; arXiv:2508.07778.

[42] NVIDIA Corporation, *CUDA Runtime API: Event Management*, 2024, accessed: 2026-01-06. [Online]. Available: https://docs.nvidia.com/cuda/cuda-runtime-api/group__CUDART__EVENT.html

[43] PyTorch Contributors, *torch.cuda.Event — PyTorch Documentation*, 2024, accessed: 2026-01-06. [Online]. Available: https://pytorch.org/docs/stable/generated/torch.cuda.Event.html

[44] B. Lim *et al.*, "Temporal Fusion Transformers for Interpretable Multi-horizon Time Series Forecasting," *International Journal of Forecasting*, vol. 37, no. 4, pp. 1748–1764, 2021.

[45] R. J. Hyndman, "Another Look at Forecast Accuracy Metrics for Intermittent Demand," *Foresight: The International Journal of Applied Forecasting*, no. 4, pp. 43–46, 2006.

[46] A. H. Murphy, "Skill Scores Based on the Mean Square Error and Their Relationships to the Correlation Coefficient," *Monthly Weather Review*, vol. 116, no. 12, pp. 2417–2424, 1988.